

# Tuning the electronic structure and magnetoresistance in a semi-metallic system by dimensional confinement

Shouvik Chatterjee,<sup>1,\*</sup> Shoaib Khalid,<sup>2,3</sup> Hadass S. Inbar,<sup>4</sup> Taozhi Guo,<sup>5</sup> Yu-Hao Chang,<sup>4</sup> Elliot Young,<sup>4</sup> Alexei V. Fedorov,<sup>6</sup> Dan Read,<sup>7</sup> Anderson Janotti,<sup>3,\*</sup> and Christopher J. Palmström<sup>1,4,\*</sup>

<sup>1</sup>*Department of Electrical & Computer Engineering,  
University of California, Santa Barbara, CA 93106, USA*

<sup>2</sup>*Department of Physics and Astronomy, University of Delaware, Newark, DE 19716, USA*

<sup>3</sup>*Department of Materials Science and Engineering,  
University of Delaware, Newark, DE 19716, USA*

<sup>4</sup>*Materials Department, University of California, Santa Barbara, CA 93106, USA*

<sup>5</sup>*Department of Physics, University of California, Santa Barbara, CA 93106, USA*

<sup>6</sup>*Advanced Light Source, Lawrence Berkeley National Laboratory, Berkeley, CA 94720, USA*

<sup>7</sup>*School of Physics and Astronomy, Cardiff University, Cardiff CF24 3AA, UK*

(Dated: January 27, 2023)

Observation of large, non-saturating magnetoresistance, tunable magnetic structure and possible realization of topologically non-trivial states make semi-metallic rare-earth monpnictides an attractive material system for basic and applied sciences. Here, utilizing a combination of angle-resolved photoemission spectroscopy, magneto-transport measurements and first-principles calculations we show that the electronic structure and material properties of these compounds can be significantly modified in few atomic layer geometries. Our observation reveals that dimensional confinement in heteroepitaxial LuSb thin films lifts the carrier compensation and differentially affects the mobility of the electron and hole-like carriers leading to a strong modification in the magnetoresistance behavior from its bulk limit, thus establishing the role of electron-hole compensation in its magnetoresistance behavior. We unambiguously establish that LuSb remains semi-metallic at least till the ultra-thin limit of 3 unit cells (1.8 nm). Observed upturn in resistivity at low temperatures in few atomic layer geometries results from strong electron-electron interaction effects and should not be construed as indicative of opening of a bulk band gap.

PACS numbers: 74.20.Rp, 74.25.Jb, 79.60.-i

Large non-saturating magnetoresistance (MR) in binary compounds of rare-earth monpnictides possessing a simple rock-salt crystal structure has generated immense interest in recent years [1–3]. Though the origin of such unusual magnetoresistance behavior is still under investigation, a combination of carrier compensation and nearly identical mobility of electron and hole-like carriers has been proposed as one of the possible reasons for such behavior to emerge [4–7]. The ability to tune the semi-metallic property and simultaneously track the modifications in magnetoresistance behavior within the same compound can potentially allow us to elucidate the role of its electronic structure on the observed magnetoresistance. Recent theoretical and experimental work suggest the possibility of stabilizing a variety of magnetic and topological phases in these compounds [8–14]. Moreover, ability to synthesize these materials in a thin film form is particularly attractive due to the possibility of easy integration in novel devices. As such, these compounds are under active investigation for potential applications [15] such as terahertz sources [16–18], plasmonics [19], thermoelectrics [20] and solar cells [21], where electronic structure and scattering processes in thin film geometries are expected to have a major influence. For example, quantum confinement in thin films of semi-metallic rare-earth monpnictides was predicted [22] to induce a phase transition from a semi-metallic to a semiconduct-

ing phase on decreasing atomic layer thickness that is yet to be established [23, 24].

To address these outstanding issues we have investigated how the electronic structure and material properties in a simple rare-earth monpnictide, LuSb, is modified in few atomic layer thick geometries. We have shown in our earlier work that the rare-earth monpnictide LuSb is a topologically trivial semi-metal, yet exhibits large non-saturating magnetoresistance and has approximately equal concentration of electron and hole-like carriers [7, 25]. Here, we utilize dimensional confinement by fabricating epitaxial thin films of LuSb of different thicknesses to differentially alter the occupation of electron and hole-like bands, which is found to have a profound influence on its magnetoresistance behavior. Though a low temperature resistivity upturn is observed in transport measurements in films of thicknesses less than 6 nm, LuSb films remain semi-metallic without any bulk band gap at least till the ultra-thin limit of 3 unit cells (1.8 nm). Insulating ground state with logarithmic divergence in resistivity is induced by strong electron interaction where the magnetoresistance behavior is dominated by both quantum interference (QI) and electron-electron interaction (EEI) effects without the opening of a bulk band gap.

Epitaxial thin films of LuSb (6.055 Å) were synthesized on nearly lattice-matched (001)-oriented GaSb substrates

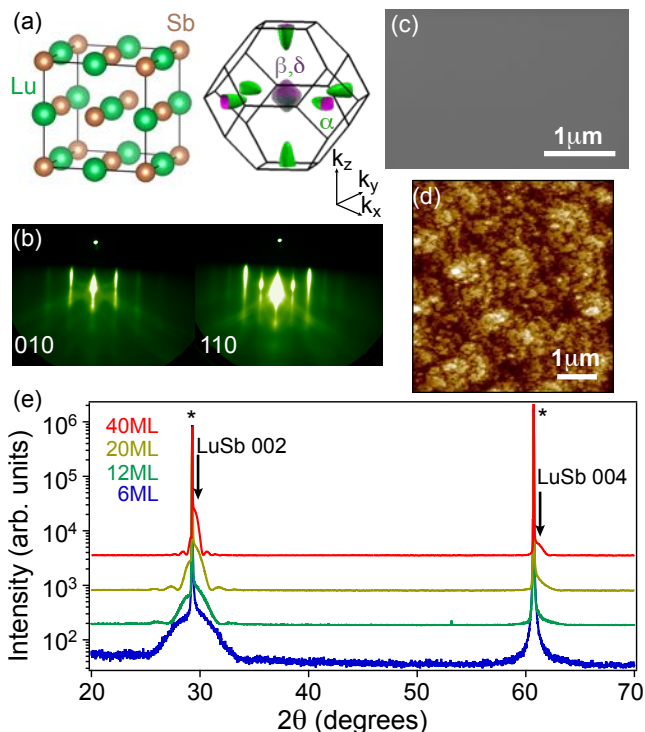


FIG. 1. Structural characterization of LuSb/GaSb (001) thin films. (a) Crystal structure of LuSb and its Fermi surface, calculated from DFT, showing two quasi-spherical hole pockets ( $\beta, \delta$ ) at the zone center and an elliptical electron pocket ( $\alpha$ ) at the zone edge. (b) RHEED images along the [010] and [110] azimuths, (c) SEM, and (d) AFM images for a 6ML thick film. Out-of-plane  $\theta$ - $2\theta$  XRD scans for epitaxial films of different thicknesses studied in this work. Substrate peaks are marked by asterisks. XRD scans are offset in intensity (along the y-axis) for clarity.

(6.09 Å) using molecular-beam epitaxy (MBE) with a base pressure better than  $5 \times 10^{-11}$  Torr. An overview of the structural characterization of these films is shown in Fig. 1. Reflection high energy electron diffraction (RHEED) shows clear  $1 \times 1$  surface reconstruction as expected from a rock-salt crystal structure. Observation of sharp 002 and 004 Bragg reflections along with finite thickness (Keissig) fringes [26] without any additional x-ray diffraction (XRD) peaks confirms that our films are single phase with abrupt surfaces and interfaces. We utilize Keissig fringes and x-ray reflectometry (XRR) to estimate film thicknesses that agree remarkably well with the nominal thickness. In addition, smooth morphology of our thin films revealed by atomic force microscopy (AFM) and scanning electron microscopy (SEM) confirms that our thin films are uniform over wide area with an RMS roughness of 0.2 nm over a  $5 \mu\text{m} \times 5 \mu\text{m}$  field of view. Further details about thin film growth and sample characterization can be found in the supplemental material [26] and in Ref. [7].

We utilized angle-resolved photoemission spectroscopy

(ARPES) to directly map out the evolution of the electronic structure of LuSb with changes in the film thickness. Epitaxial thin films were transferred into the measurement chamber in a custom-built vacuum suitcase with pressure better than  $1 \times 10^{-10}$  Torr. In Fig. 2, we show the hole and the electron pockets at  $\Gamma$  and bulk  $X$  point ( $\bar{M}$  at the surface Brillouin zone), respectively. The occupation of the hole pockets decreases dramatically as the film thickness is reduced, whereas no significant change in the occupation of the electron pocket is observed for all but 6ML thick film. For the 6ML thick film we observe a reduction in ellipticity ( $e = \frac{k_{F, \text{semimajor}}}{k_{F, \text{semiminor}}}$ ) of the electron pocket with  $k_{F, \text{semiminor}}$  remaining unchanged from the bulk limit. Our ARPES measurements clearly reveal that finite occupation is maintained for both the electron and hole like bands, thereby preserving the semi-metallic character of LuSb even at the ultra-thin limit of 6 monolayers (ML), consistent with our density functional theory (DFT) calculations [27–32]. However, our slab calculations predict strong uplift of the electron pocket at  $\bar{M}$  towards the Fermi level as the film thickness is reduced (Fig. S8(a)-(d) in supplemental material [26]). Reasonable agreement with the experimental results is obtained by assuming an additional charge of 0.5 electrons per unit-cell area in the LuSb film, as shown in Fig. S8(e)-(h) [26]. One plausible origin of such excess charge is the Ga-LuSb(001) termination at the interface between the Ga terminated GaSb and LuSb atomic layers [33]. These excess charge carriers will end up in the LuSb film due to the positive Schottky barrier height at the GaSb/LuSb interface, which can explain the observed trend in our ARPES data (see supplemental material [26] for a more detailed discussion).

Finite thickness of our films results in the formation of quantum well states as seen for the hole-like carriers in 20, 12, and 6ML samples. Separation between the energy levels in quantum well states for a particular film thickness is inversely proportional to the effective mass of the carriers. The 40ML thick film is a compensated semi-metal with equal concentration of electron ( $n = 3.22 \times 10^{20} \text{ cm}^{-3}$ ) and hole-like carriers ( $p = 3.18 \times 10^{20} \text{ cm}^{-3}$ ) and their ratio  $\frac{n}{p} \approx 1.01$ . However, thinner films are not carrier compensated with the ratio being approximately equal to 2.83 for 6ML thick film even considering finite occupation for only the lowest sub-band of the in-plane electron pockets (along  $k_x$  and  $k_y$  with confinement along  $k_z$ , see Fig. 1 (a)). In order to estimate the effective mass of the carriers near the Fermi level, we have enumerated the mass enhancement factor defined as

$$\tilde{m} = \frac{\partial E_{DFT} / \partial k}{\partial E_{film} / \partial k} \Big|_{k=k_{F, film}} = \frac{v_{DFT}}{v_{film}} \quad (1)$$

where  $v_{DFT}$  and  $v_{film}$  are Fermi velocity estimated from hybrid DFT of bulk LuSb and measured Fermi velocity, respectively, both calculated at the same Fermi wave vector  $k_{F, film}$ . Higher sub-band states generated by quantum confinement were found to have higher effective mass for a particular film thickness. This increase in effective

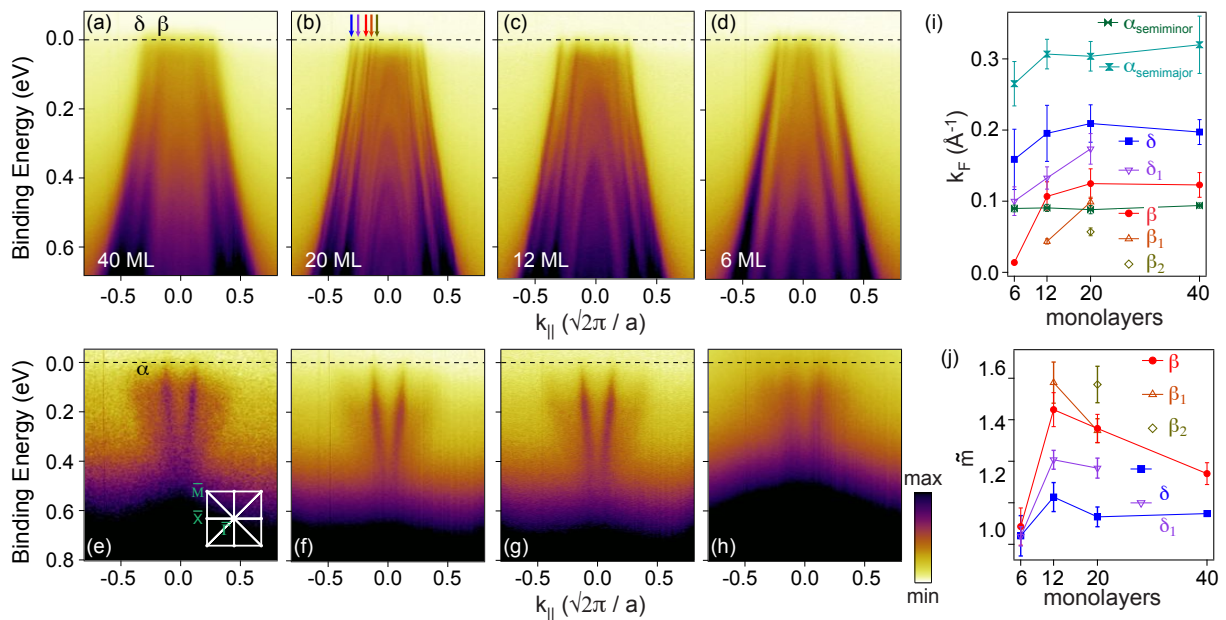


FIG. 2. ARPES of LuSb/GaSb (001) thin films.  $E$ - $k$  spectral map at the bulk  $\Gamma$  point (top panels) along  $\bar{M} - \bar{\Gamma} - \bar{M}$  of the surface Brillouin zone for thin films of thickness (a) 40 ML (b) 20ML (c) 12 ML and (d) 6 ML, and at the bulk  $X$  point (bottom panels) along  $\bar{\Gamma} - \bar{M} - \bar{\Gamma}$  of the surface Brillouin zone for (e) 40 ML (f) 20ML (g) 12 ML and (h) 6 ML thick films. (i) Extracted Fermi wavevectors  $k_F$  for  $\alpha$ ,  $\beta$  and  $\delta$  pockets as a function of film thickness. (j) Mass enhancement factor  $\tilde{m}$ , as defined in the main text, measured along  $\bar{M} - \bar{\Gamma} - \bar{M}$  for different film thicknesses. Surface Brillouin zone of LuSb is shown in the inset of panel (e)

mass most likely follows from finite  $k_z$  sampling in ultra-thin films due to non-parabolic character of the hole-like carriers as has also been observed in other material systems [34]. However, effective mass of all the hole-like carriers decrease for the 6ML thick film with the effect being particularly pronounced for the  $\beta$  pocket. This could be due to a combination of several factors such as lower occupation of the hole-like bands in the 6ML thick film bringing them closer to a parabolic character and also due to lattice distortions arising at the LuSb-GaSb interface, which is expected to have a stronger influence in thinner films.

The changes in the electronic structure with film thickness in LuSb were found to have a significant impact on its transport properties. Transport measurements were carried out utilizing standard low frequency lock-in technique with an excitation current of  $10\mu\text{A}$  using Hall bar devices with dimensions  $400\mu\text{m} \times 100\mu\text{m}$ . Evolution of the temperature dependence of resistance with film thickness is shown in Fig. 3 (a). While both 40 and 20ML thick films exhibit metallic behavior, a low temperature resistivity upturn can be seen in 12 and 6ML films. This might be construed as indicative of a semiconducting behavior with a bulk band gap in these films, which however is not the case as has been unambiguously revealed by our ARPES data in Fig. 2. We will examine the origin of such a transport behavior in the later part of this work. Magnetoresistance in these films undergo a dramatic change both in magnitude and shape with film

thickness. While 40ML thick film exhibits a MR of 120% at 14T, it drops down to less than 10% in the thinner films, with the 6ML film showing a saturating behavior at high field values unlike the thicker films due to strong EEI effects [26]. Shubnikov deHaas oscillations (SdH) were observed for all the electronic bands ( $\alpha$ ,  $\beta$ ,  $\delta$ ) for the 40ML thick film, however only  $\alpha$  and  $\beta$  Fermi surfaces exhibited SdH oscillations for the 20ML thick film. SdH oscillations were not observed in the thinner films indicating an overall reduction in mobility with decreasing film thickness. Estimated effective masses for the  $\alpha$ ,  $\beta$  and  $\delta$  pockets in 40ML thick films were found to be in close agreement with the results from DFT calculations in the bulk limit [7]. Quantum mobilities were estimated to be  $4.04 \times 10^3 \text{ cm}^2/\text{Vs}$ ,  $2.2 \times 10^3 \text{ cm}^2/\text{Vs}$ ,  $7.79 \times 10^2 \text{ cm}^2/\text{Vs}$  for the  $\alpha$ ,  $\beta$  and  $\delta$  pockets, respectively in 40ML thick films that decreases to  $6.57 \times 10^2 \text{ cm}^2/\text{Vs}$  and  $5.04 \times 10^2 \text{ cm}^2/\text{Vs}$  for the  $\alpha$  and  $\beta$  pockets in 20ML thick films, a drop of 84% and 77%, respectively [26]. An analysis of the oscillation frequencies further indicates a reduction in the Fermi wave vector ( $k_F$ ) in 20ML thick films by  $0.007 \pm 0.001$  for the  $\beta$  pocket and a very tiny reduction of  $0.001 \pm 0.001$  for the  $\alpha$  pocket, in agreement with our ARPES data. Our ARPES and quantum oscillation measurements reveals a differential decrease in mobility and carrier concentration between the electron and hole-like carriers with decreasing film thickness that explains the observed evolution from multi-carrier Hall behavior in 40ML thick film to a single carrier electron-

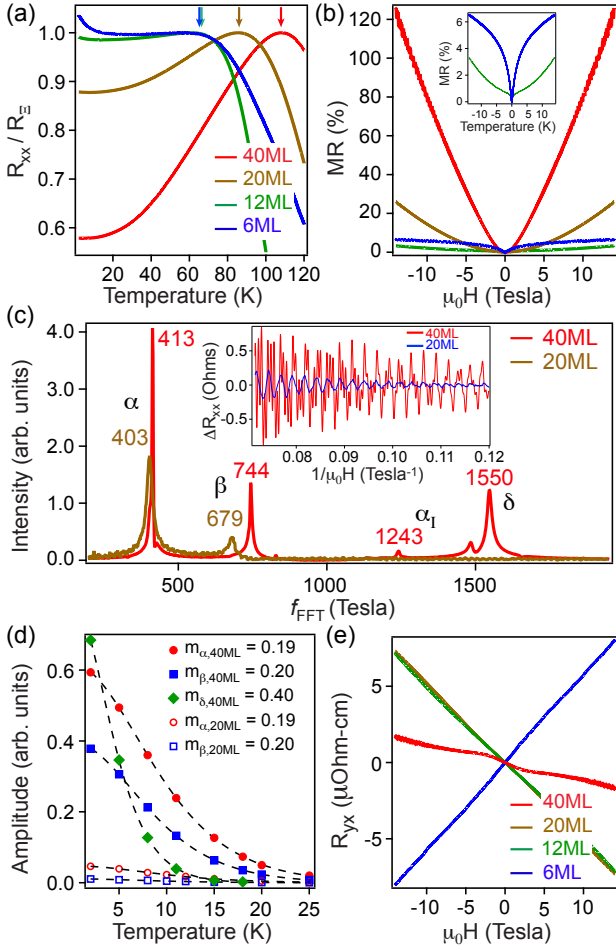


FIG. 3. Transport properties of LuSb/GaSb (001) thin films. (a) Temperature dependence of resistance in thin films of various thicknesses.  $R_{\Xi}$  is the resistance at the sample temperature below which film resistance is dominated by LuSb layers. Temperatures corresponding to  $R_{\Xi}$  are indicated for all film thicknesses. (b) Evolution of magnetoresistance with film thickness. Inset highlights saturating magnetoresistance behavior at high fields for 6ML thick sample. (c) Fast Fourier Transform (FFT) of the quantum oscillations for 40 and 20ML thick films. Corresponding resistance oscillations are shown in inset.  $\beta$  and  $\delta$  are the hole pockets at the zone center.  $\alpha$  and  $\alpha_I$  are the frequencies corresponding to the projection of the elliptical electron pockets along the magnetic field direction ( $k_z$ ) and those lying in the plane perpendicular to it ( $k_x, k_y$ ), respectively, as shown in Fig. 1 (a). (d) Extracted effective mass of carriers from quantum oscillations for 40 and 20ML thick film. (e) Hall resistance as a function of film thickness.

like behavior in thinner films of 20 and 12ML. However, completely opposite behavior is observed for 6ML thick film, which exhibits a p-type Hall conductivity despite a smaller carrier concentration of hole-like carriers as has been revealed in our ARPES data indicating rapid reduction in mobility of the electron-like carriers in 6ML thick film. This is most likely due to the enhancement in surface scattering for the electron-like carriers in 6ML thick

film as the Fermi wavevector ( $k_F$ ) along the semi-minor axis of the elliptical electron pocket now becomes smaller than  $\pi/t$ ,  $t$  being the film thickness in contrast to the case of the thicker films. This is in accord with our previous observation of the change in sign of the Hall voltage on introduction of extended defects in thicker films, which most likely is a result of differential increase in scattering for the electron-like carriers [7]. Furthermore, our observation of the decrease in effective mass of the hole-like bands in 6ML thick film can also lead to a relative enhancement in hole mobility contributing to the observed p-type Hall conductivity.

Having established the changes in the electronic structure and its broad impact on transport properties we now examine the semiconducting-like behavior at low temperatures observed in thinner films. In Fig. 4 (a) and (b) we show a logarithmic drop in conductance with temperature for the 6 and 12 ML thick films, respectively. Both QI effects such as weak localization and EEI effects can give rise to such a behavior in the two-dimensional limit [35–37]. To distinguish between the two cases we examine the change in slope in the temperature dependence of conductance as a function of applied magnetic field. QI effects can be readily suppressed on application of magnetic field, while EEI effects are more robust due to larger characteristic fields [35, 38]. Therefore, the pre-factor  $A$  obtained at high field values  $A_{high}$  is solely due to EEI effects  $A_{high} = A_{ee}$ , whereas the one at zero field is a combination of both QI ( $A_{QI}$ ) and EEI effects ( $A_{ee}$ ),  $A_{low} = A_{ee} + A_{QI}$ . We estimate  $A_{QI}$  to be -0.09 and -0.33 and  $A_{ee}$  equal to 0.45 and 0.83 for 12 and 6ML thick film, respectively. We obtain a negative value for  $A_{QI}$  for both 12 and 6ML thick film, consistent with the observation of weak anti-localization (WAL) behavior in magnetoresistance, shown in Figs. 4 (d-e). This is not surprising as the importance of strong spin-orbit scattering in LuSb has already been revealed in our previous work [7]. Angular dependence of magnetoresistance confirms the two-dimensional character of WAL, while further distinguishing it from the effects of Zeeman splitting of the EEI correction that also results in a dip in zero-field magnetoresistance but is insensitive to the magnetic field direction at low fields [35, 38]. Simultaneous occurrence of both EEI and QI effects in our LuSb thin films is also not surprising due to their different origins and has been seen in various other thin films including those of topological insulators[39–42]. Having established that the low field magnetoresistance behavior is dominated by weak antilocalization effect, we investigate the scattering mechanisms in these films utilizing Hikami-Larkin-Nagaoka (HLN) theory[43] applicable for a two-dimensional electronic system, given by:

$$\Delta G_{WAL}(B) = \alpha \frac{e^2}{\pi h} \left[ \frac{1}{2} \left( \Psi \left( \frac{1}{2} + \frac{B_{\phi}}{B} \right) - \ln \left( \frac{B_{\phi}}{B} \right) \right) - \frac{3}{2} \left( \Psi \left( \frac{1}{2} + \frac{\frac{4}{3} B_{SO} + B_{\phi}}{B} \right) - \ln \left( \frac{\frac{4}{3} B_{SO} + B_{\phi}}{B} \right) \right) \right], \quad (2)$$

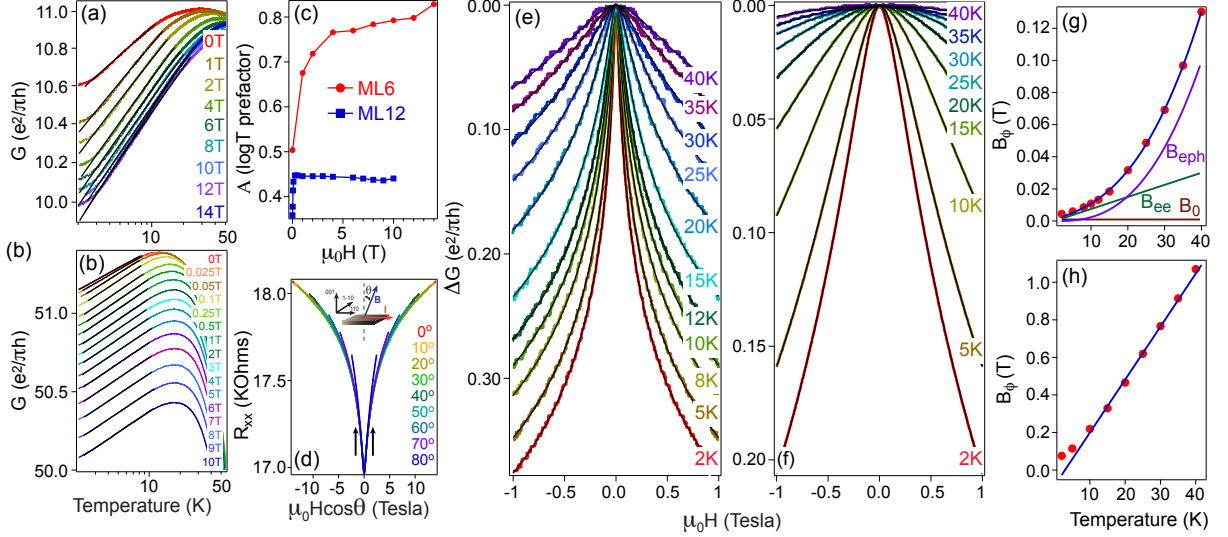


FIG. 4. QI and EEI effects in ultra-thin LuSb/GaSb (001) thin films. Temperature dependence of conductance in (a) 6 and (b) 12 ML thick films. Logarithmic fits to the conductance are shown in black. (c) Variation of the prefactor of the logarithmic dependence of conductance extracted from the fits in (a) and (b) as a function of applied magnetic field. (d) Resistance of a 6 nm thick film plotted against the perpendicular component of the magnetic field vector for different angle values. The angle is defined in the inset. Arrows indicate that between  $\mu_0 H = \pm 1$  T, magnetoresistance curves obtained at different angular configurations fall on one another establishing the two-dimensional nature of the quantum interference effect. Differential conductance  $\Delta G(B = \mu_0 H) = G(B) - G(0)$  as a function of magnetic field and corresponding HLN fits for (e) 12 and (f) 6 ML thick films. Temperature dependence of the extracted dephasing field as a function of temperature for (g) 12 and (h) 6 ML thick films. Contribution of  $B_{ee}$ ,  $B_{eph}$  and  $B_0$  to  $B_\phi$  in (g) are shown in green, violet and brown, respectively.

where  $B_\phi$  and  $B_{SO}$  are the characteristic fields corresponding to inelastic and spin-orbit scattering, respectively and  $\Psi(x)$  is the digamma function. Fits to the magnetoconductance data is shown in Fig. 4 (e) and (f) and extracted temperature dependence of the characteristic dephasing field  $B_\phi$  for 12 and 6 ML films are shown in Figs. 4(g) and (h), respectively. At 2K, phase coherence lengths are found to be 193 nm and 47 nm and spin-orbit scattering lengths, 11 nm and 10 nm for 12 and 6ML thick films, respectively [26]. Factors contributing to the dephasing field  $B_\phi$  can be separated by examining its temperature dependence. While the electron-electron scattering is expected to have a linear temperature dependence for a 2-dimensional system, electron-phonon scattering increases as  $T^n$ , where  $n$  varies between 2 and 4 [44]. Temperature dependence of  $B_\phi$  for the 12 ML thick film can be well approximated as

$$B_\phi = B_0 + B_{ee} + B_{eph} = a + bT + cT^n, \quad (3)$$

where  $B_0$ ,  $B_{ee}$ , and  $B_{eph}$  are contributions due to impurity, electron-electron, and electron-phonon scattering, respectively and  $a$ ,  $b$ , and  $c$  are constants. As expected, at low temperatures electron-electron scattering dominates, which is quickly overwhelmed by contributions from electron-phonon scattering at higher temperatures, which is found to have a  $T^{2.2}$  dependence. However, for the 6 ML thick film,  $B_\phi$  shows a linear temperature dependence suggesting the predominance of EEI effects in

thinner films and also much weaker electron-phonon scattering. Our observation thus explains the emergence of semiconductor-like behavior at low temperatures in these films despite the absence of a bulk band gap.

In summary, we have shown how magnetoresistance behavior can be modified and charge compensation can be lifted in an otherwise compensated semimetallic system by dimensionally confining charge carriers in ultra-thin films. Both charge compensation and mobility were found to play a predominant role responsible for the magnetoresistance behavior in LuSb thin films. Though, electronic structure and occupation of charge carriers can be significantly modified in the ultra-thin limit, no evidence for the lifting of semi-metallicity is found in these thin heteroepitaxial films. Our measurements further highlight the inadequacy of transport measurements alone in understanding the predicted semi-metallic to semiconducting phase transition or the evolution of the electronic structure with film thickness as QI and EEI effects along with differential carrier mobilities of the electron and hole-like carriers significantly affects the transport behavior in thin films consisting of only a few atomic layers. Our work sets the stage for further control over electronic properties in semi-metallic systems by application of bi-axial stress, proximity effect and artificial heterostructures.

## ACKNOWLEDGMENTS

Synthesis of thin films, development of the UHV suite, ARPES experiments, and theoretical work were supported by the US Department of Energy (Contract No. DE-SC0014388). Development of the growth facilities and low temperature magnetotransport measurements were supported by the Office of Naval Research through the Vannevar Bush Faculty Fellowship under the Award No. N00014-15-1-2845. This research used resources of the Advanced Light Source, which is a DOE Office of Science User Facility under contract no. DE-

AC02-05CH11231. We acknowledge the use of facilities within the National Science Foundation Materials Research and Engineering Center (DMR 11-21053) at the University of California at Santa Barbara, the LeRoy Eyring Center for Solid State Science at Arizona State University. Density functional theory calculations made use of the Extreme Science and Engineering Discovery Environment, NSF Grant No. ACI-1053575, and high-performance computing and the Information Technologies resources at the University of Delaware. D.R. gratefully acknowledges support from the Leverhulme Trust via an International Academic Fellowship (IAF-2018-039).

- 
- \* Authors to whom correspondence should be addressed: schatterjee@ucsb.edu, cjpalm@ucsb.edu, janotti@udel.edu
- [1] Tafti, F., Gibson, Q., Kushwaha, S., Haldolaarachchige, N. & Cava, R. J. Resistivity plateau and extreme magnetoresistance in LaSb. *Nature Physics* **12**, 272 (2016).
  - [2] Tafti, F. F. *et al.* Temperature- field phase diagram of extreme magnetoresistance. *Proceedings of the National Academy of Sciences* **113**, E3475–E3481 (2016).
  - [3] Ye, L., Suzuki, T., Wicker, C. R. & Checkelsky, J. G. Extreme magnetoresistance in magnetic rare-earth monpnictides. *Physical Review B* **97**, 081108 (2018).
  - [4] Xu, J. *et al.* Origin of the extremely large magnetoresistance in the semimetal YSb. *Physical Review B* **96**, 075159 (2017).
  - [5] Zeng, L.-K. *et al.* Compensated semimetal LaSb with unsaturated magnetoresistance. *Physical Review Letters* **117**, 127204 (2016).
  - [6] He, J. *et al.* Distinct electronic structure for the extreme magnetoresistance in YSb. *Physical Review Letters* **117**, 267201 (2016).
  - [7] Chatterjee, S. *et al.* Weak antilocalization in quasi-two-dimensional electronic states of epitaxial LuSb thin films. *Physical Review B* **99**, 125134 (2019).
  - [8] Zeng, M. *et al.* Topological semimetals and topological insulators in rare earth monpnictides. *arXiv preprint arXiv:1504.03492* (2015).
  - [9] Khalid, S., Sabino, F. P. & Janotti, A. Topological phase transition in LaAs under pressure. *Physical Review B* **98**, 220102 (2018).
  - [10] Li, Z. *et al.* GdN thin film: Chern insulating state on square lattice. *Physical Review B* **92**, 201303 (2015).
  - [11] Inoue, H. *et al.* Band engineering of a magnetic thin film rare-earth monpnictide: A platform for high Chern number. *Physical Review Materials* **3**, 101202 (2019).
  - [12] Xu, J. *et al.* Orbital-flop induced magnetoresistance anisotropy in rare earth monpnictide CeSb. *Nature Communications* **10**, 1–8 (2019).
  - [13] Wu, F. *et al.* Anomalous quantum oscillations and evidence for a non-trivial Berry phase in SmSb. *NPJ Quantum Materials* **4**, 20 (2019).
  - [14] Nayak, J. *et al.* Multiple dirac cones at the surface of the topological metal LaBi. *Nature Communications* **8**, 13942 (2017).
  - [15] Bomberger, C. C., Lewis, M. R., Vanderhoef, L. R., Doty, M. F. & Zide, J. M. Overview of lanthanide pnictide films and nanoparticles epitaxially incorporated into III-V semiconductors. *Journal of Vacuum Science & Technology B, Nanotechnology and Microelectronics: Materials, Processing, Measurement, and Phenomena* **35**, 030801 (2017).
  - [16] Salas, R. *et al.* Growth and properties of rare-earth arsenide InGaAs nanocomposites for terahertz generation. *Applied Physics Letters* **106**, 081103 (2015).
  - [17] Bjarnason, J. *et al.* ErAs: GaAs photomixer with two-decade tunability and 12  $\mu$ w peak output power. *Applied Physics Letters* **85**, 3983–3985 (2004).
  - [18] Sukhotin, M. *et al.* Photomixing and photoconductor measurements on ErAs/InGaAs at 1.55  $\mu$ m. *Applied Physics Letters* **82**, 3116–3118 (2003).
  - [19] Krivoy, E. M. *et al.* Rare-earth monpnictide alloys for tunable, epitaxial, designer plasmonics. *ACS Photonics* **5**, 3051–3056 (2018).
  - [20] Liu, X. *et al.* Properties of molecular beam epitaxially grown ScAs: InGaAs and ErAs: InGaAs nanocomposites for thermoelectric applications. *Journal of Crystal Growth* **316**, 56–59 (2011).
  - [21] Zide, J. *et al.* Increased efficiency in multijunction solar cells through the incorporation of semimetallic ErAs nanoparticles into the tunnel junction. *Applied Physics Letters* **88**, 162103 (2006).
  - [22] Sandomirskii, V. Quantum size effect in a semimetal film. *Sov. Phys. JETP* **25**, 101 (1967).
  - [23] Allen Jr, S. *et al.* Magneto-transport in ultrathin ErAs epitaxial layers buried in GaAs. *Surface Science* **228**, 13–15 (1990).
  - [24] Kawasaki, J. K. *et al.* Local density of states and interface effects in semimetallic eras nanoparticles embedded in gaas. *Physical Review Letters* **107**, 036806 (2011).
  - [25] Pavlosiuk, O., Kleinert, M., Swatek, P., Kaczorowski, D. & Wiñiewski, P. Fermi surface topology and magnetotransport in semimetallic LuSb. *Scientific Reports* **7**, 12822 (2017).
  - [26] Supplementary information .
  - [27] Khalid, S., Sharan, A. & Janotti, A. Hybrid functional calculations of electronic structure and carrier densities in rare-earth monpnictides. *arXiv preprint arXiv:1911.06184* (2019).

- [28] Kresse, G. & Hafner, J. Ab initio molecular dynamics for liquid metals. *Physical Review B* **47**, 558 (1993).
- [29] Kresse, G. & Hafner, J. Ab initio molecular-dynamics simulation of the liquid-metal–amorphous-semiconductor transition in germanium. *Physical Review B* **49**, 14251 (1994).
- [30] Blöchl, P. Projector augmented-wave method. *Physical Review B* **50**, 17953 (1994).
- [31] Heyd, J., Scuseria, G. E. & Ernzerhof, M. Hybrid functionals based on a screened Coulomb potential. *Journal of Chemical Physics* **118**, 8207–8215 (2003).
- [32] Heyd, J., Scuseria, G. E. & Ernzerhof, M. Erratum: Hybrid functionals based on a screened Coulomb potential [J. Chem. Phys. 118, 8207 (2003)]. *Journal of Chemical Physics* **124**, 219906 (2006).
- [33] Tarnow, E. Structure of the interface between ErAs, a cubic semimetal and AlAs, a tetrahedral semiconductor. *Journal of applied physics* **77**, 6317–6326 (1995).
- [34] Kawasaki, J. K. *et al.* Engineering carrier effective masses in ultrathin quantum wells of IrO<sub>2</sub>. *Physical Review Letters* **121**, 176802 (2018).
- [35] Lee, P. A. & Ramakrishnan, T. Disordered electronic systems. *Reviews of Modern Physics* **57**, 287 (1985).
- [36] Bergmann, G. Weak localization in thin films: a time-of-flight experiment with conduction electrons. *Physics Reports* **107**, 1–58 (1984).
- [37] Altshuler, B. L., Aronov, A. G. & Lee, P. Interaction effects in disordered fermi systems in two dimensions. *Physical Review Letters* **44**, 1288 (1980).
- [38] Altshuler, B. L. & Aronov, A. G. Electron–electron interaction in disordered conductors. In *Modern Problems in Condensed Matter Sciences*, vol. 10, 1–153 (Elsevier, 1985).
- [39] Breznay, N. P. *et al.* Weak antilocalization and disorder-enhanced electron interactions in annealed films of the phase-change compound GeSb<sub>2</sub>Te<sub>4</sub>. *Physical Review B* **86**, 205302 (2012).
- [40] Wang, L. *et al.* Tuning magnetotransport in a compensated semimetal at the atomic scale. *Nature Communications* **6**, 8892 (2015).
- [41] Hu, J. *et al.* Enhanced electron coherence in atomically thin Nb<sub>3</sub>SiTe<sub>6</sub>. *Nature Physics* **11**, 471 (2015).
- [42] Liu, M. *et al.* Electron interaction-driven insulating ground state in bi 2 se 3 topological insulators in the two-dimensional limit. *Physical Review B* **83**, 165440 (2011).
- [43] Hikami, S., Larkin, A. I. & Nagaoka, Y. Spin-orbit interaction and magnetoresistance in the two dimensional random system. *Progress of Theoretical Physics* **63**, 707–710 (1980).
- [44] Lin, J.-J. & Bird, J. Recent experimental studies of electron dephasing in metal and semiconductor mesoscopic structures. *Journal of Physics: Condensed Matter* **14**, R501 (2002).

## Supplemental Material: Tuning the electronic structure and magnetoresistance in a semi-metallic system by dimensional confinement

Shouvik Chatterjee,<sup>1,\*</sup> Shoaib Khalid,<sup>2,3</sup> Hadass S. Inbar,<sup>4</sup> Taozhi Guo,<sup>5</sup> Yu-Hao Chang,<sup>4</sup> Elliot Young,<sup>4</sup> Alexei V. Fedorov,<sup>6</sup> Dan Read,<sup>7</sup> Anderson Janotti,<sup>3,\*</sup> and Christopher J. Palmstrøm<sup>1,4,\*</sup>

<sup>1</sup>*Department of Electrical & Computer Engineering,  
University of California, Santa Barbara, CA 93106, USA*

<sup>2</sup>*Department of Physics and Astronomy, University of Delaware, Newark, DE 19716, USA*

<sup>3</sup>*Department of Materials Science and Engineering,  
University of Delaware, Newark, DE 19716, USA*

<sup>4</sup>*Materials Department, University of California, Santa Barbara, CA 93106, USA*

<sup>5</sup>*Department of Physics, University of California, Santa Barbara, CA 93106, USA*

<sup>6</sup>*Advanced Light Source, Lawrence Berkeley National Laboratory, Berkeley, California 94720, USA*

<sup>7</sup>*School of Physics and Astronomy, Cardiff University, Cardiff CF24 3AA, UK*

(Dated: January 27, 2023)

## I. THIN FILM GROWTH AND ESTIMATION OF FILM THICKNESS:

Epitaxial thin films of LuSb were synthesized by molecular-beam epitaxy (MBE) in MOD Gen II growth chamber at 315 °C by co-depositing Lu and Sb from Langmuir effusion cells with Lu to Sb flux ratio set at 1:1.1. Samples of different thicknesses were grown under the same conditions on the same day. Prior to LuSb growth, 5 nm thick GaSb buffer layer was grown at 450 °C under  $Sb_4$  overpressure on low n-type doped (001) GaSb substrates that freezes out at low temperatures. Native oxide was desorbed from GaSb substrates using atomic hydrogen. Before growth, atomic fluxes of Lu and Sb were determined by *in situ* beam flux measurements using an ion gauge that allowed to synthesize thin films of different nominal thicknesses by adjusting the growth time. Beam flux measurements were calibrated by Rutherford backscattering spectrometry (RBS) by measuring the elemental area density of calibration samples on Si. Sample surfaces were protected by 10 nm thick  $AlO_x$  layer deposited *in vacuo* using e-beam evaporation before taking the samples out of the UHV chamber. For ARPES measurements conductive n-type Te doped GaSb (001) substrates were used.

To confirm thickness of our thin films we utilized both high-resolution x-ray diffraction where Keissig fringes could be observed around LuSb (002) diffraction peak as shown in Fig. S1 and x-ray reflectivity measurements shown in Fig. S2. From angular position of the Keissig fringes film thickness  $t$  can be obtained as

$$t = \frac{\lambda}{2\Delta w \cos(\theta_B)} \quad (S1)$$

where  $\Delta w$  is the difference in angle between two adjacent diffraction peaks and  $\theta_B$  is the Bragg angle corresponding to LuSb (002) diffraction peak. Our estimated film thicknesses are in excellent correspondence with the nominal thickness values.

## II. EXTRACTION OF FERMI WAVEVECTOR AND EFFECTIVE MASS CALCULATION

Both Fermi wavevector and Fermi velocity is obtained from a linear fit of the band dispersion along  $\bar{M} - \Gamma - \bar{M}$  close to the Fermi level within an energy range of 100 meV, measured using angle-resolved photoemission spectroscopy (ARPES). The band dispersion is extracted from momentum-distribution curves (MDCs). Extracted band dispersion and corresponding linear fits are shown in Fig. S3. Mass enhancement factors were determined using the extracted Fermi velocity from the fits as described in the main text.

## III. ESTIMATION OF EFFECTIVE MASS AND QUANTUM MOBILITY

Quantum oscillations were observed in 40 and 20ML thick films. To reliably extract effective mass and quantum mobility in this multi-band system, oscillations corresponding to individual frequencies were obtained by application of inverse Fourier transform on individual frequencies extracted using a band-pass filter on the fast Fourier transform data from the whole film, shown in Fig. 3(c) in the main text. According to Lifshitz-Kosevich formula

$$\frac{\Delta R}{R(0)} \propto R_T R_D R_S \cos[2\pi(\frac{f}{\mu_0 H} - \gamma - \delta)] \quad (S2)$$

where  $R_T$ ,  $R_H$ , and  $R_S$  are temperature, field, and spin dependent damping factors. Effective mass is calculated from the temperature dependent damping of oscillation amplitude at a particular magnetic field given by

$$R_T = \frac{(2\pi^2 k_B m^* T / e \hbar \mu_0 H)}{\text{Sinh}(2\pi^2 k_B m^* T / e \hbar \mu_0 H)}. \quad (S3)$$

Field-dependent damping parameter  $R_H$  in Eq. S2 is given by

$$R_H = e^{-\pi / \mu_q \mu_0 H}, \quad (S4)$$

where  $\mu_q$  is the quantum mobility. Thus, once  $m^*$  is determined using Eq. S3, assuming  $R_S$  is independent of magnetic field,  $\mu_q$  can be determined from the slope of  $\ln(\frac{\Delta R}{R(0)} \times 1/R_T)$  plotted against  $1/\mu_0 H$  as shown in Fig. S4

#### IV. COMPUTATIONAL APPROACH AND RESULTS

Our first-principles calculations are based on the density functional theory (DFT) and projector augmented wave (PAW)[1] method as implemented in the VASP code[2, 3]. For the exchange and correlation we employed both the generalized gradient approximation (GGA) of Perdew-Burke-Ernzerhof [4] and screened hybrid functional (HSE06)[5, 6]. The exchange potential in HSE06 is divided into short range and long range parts separated by a screening parameter of ( $\omega = 0.20 \text{ \AA}^{-1}$ ). In the short range part the Hartree-Fock exchange and GGA exchange are mixed with a ratio 25:75. In the long range part only GGA exchange is used. The PAW potential for Sb contains five valence electrons,  $5s^25p^3$ , and for Lu, it contains 9 valence electrons,  $5p^66s^25d^1$ . The inclusion of localized  $4f$  orbitals in Lu shows up a dispersionless band at around 8 eV below Fermi level with less than 5% change in carrier concentration based on test calculations.

First we calculated the electronic band structure of bulk LuSb using the tetragonal cell with 4 atoms corresponding to the smallest cell that can represent the (001) surface of LuSb. We performed calculations using DFT-GGA and HSE06 for comparison, as shown in Fig. S7. These calculations were performed using a  $8 \times 8 \times 6$   $\Gamma$ -centered mesh of special  $k$ -points. The effects of spin-orbit coupling (SOC) are included in all band structure calculations. As recently reported [7], we find that the GGA functional overestimates the overlap between the electron and hole pockets, in analogy to the well-known underestimation of band gap in semiconductors and insulators. This overestimation leads to higher carrier concentrations and Fermi wavevectors when using DFT-GGA functional, while the HSE06 functional gives results in very good agreement with experimental data [8].

We then carried out calculations for LuSb(001) slabs, for 6, 12, 20, and 40 monolayers (ML). These calculations were performed using the DFT-GGA functional with  $12 \times 12 \times 1$  special  $k$ -points; HSE06 calculations for these slabs are prohibitively expensive given the size of the supercell and the large number of  $k$ -points required to describe metallic systems. The results are shown in Fig. S8, where we used the Fermi level as reference. We note that the electron pocket at  $\Gamma$  seen in the bulk (Fig. S7) and in the surface band structures (Fig. S8) are projections of the pockets at the  $X_3$  in the bulk primitive cell (2 atoms/per cell) that is folded to  $\Gamma$  in the bulk using the 4-atom tetragonal unit cell and the slabs [9]. We can see that the electron pocket at  $\bar{M}$  is strongly affected by quantum confinement, contrary to the experimental data shown in Fig. 2 in the main text. We explain this discrepancy by the excess charge due to specific termination at the interface between the LuSb(001) film and the GaSb(001) substrate. Considering a Ga-LuSb termination at the interface, we expect an excess charge at the interface to be accommodated in the LuSb film, since the Fermi level of LuSb lies in the gap of GaSb [7]. Good agreement between ARPES and DFT calculations, correcting for the DFT-GGA overestimation, is obtained after adding 0.5 electrons per unit cell area to the LuSb slabs, assuming a rigid-band filling. As a consequence of this excess charge, we can see that the minimum of the electron pocket at  $\bar{M}$  remains almost unchanged with respect to the Fermi level, while the maximum of the hole pocket at  $\Gamma$  significantly decreases, in agreement with the ARPES measurements shown in Fig. 2 (main text). The variation of the maximum of the hole pocket at  $\Gamma$  and minimum of the electron pocket at  $\bar{M}$  as a function of number of layers of LuSb is shown in Fig. S9. Note that we don't exclude the possibility that a part of the excess electrons due to the interface termination remains trapped at surface states in the experiment.

Finally, in Fig. S10 we show the calculated Fermi wave vector of the hole pockets  $\beta$  and  $\delta$ , and electron pockets  $\alpha$  at  $\bar{M}$  for the various thickness of the LuSb slab. This is to be compared to the experimental results shown in Fig. 2(i) (main text). The agreement is overall good, considering that the DFT-GGA calculations overestimate the overlap of the electron and hole pockets and, consequently, the Fermi wavevectors as well.

---

\* Authors to whom correspondence should be addressed: schatterjee@ucsb.edu, cjpalm@ucsb.edu, janotti@udel.edu

- [1] Blöchl, P. Projector augmented-wave method. *Physical Review B* **50**, 17953 (1994).
- [2] Kresse, G. & Hafner, J. Ab initio molecular dynamics for liquid metals. *Physical Review B* **47**, 558 (1993).
- [3] Kresse, G. & Hafner, J. Ab initio molecular-dynamics simulation of the liquid-metal–amorphous-semiconductor transition in germanium. *Physical Review B* **49**, 14251 (1994).
- [4] Perdew, J. P., Burke, K. & Ernzerhof, M. Generalized gradient approximation made simple. *Physical Review Letters* **77**, 3865 (1996).
- [5] Heyd, J., Scuseria, G. E. & Ernzerhof, M. Hybrid functionals based on a screened Coulomb potential. *Journal of Chemical Physics* **118**, 8207–8215 (2003).
- [6] Heyd, J., Scuseria, G. E. & Ernzerhof, M. Erratum: Hybrid functionals based on a screened Coulomb potential [J. Chem. Phys. 118, 8207 (2003)]. *Journal of Chemical Physics* **124**, 219906 (2006).
- [7] Khalid, S., Sharan, A. & Janotti, A. Hybrid functional calculations of electronic structure and carrier densities in rare-earth monpnictides. *arXiv preprint arXiv:1911.06184* (2019).

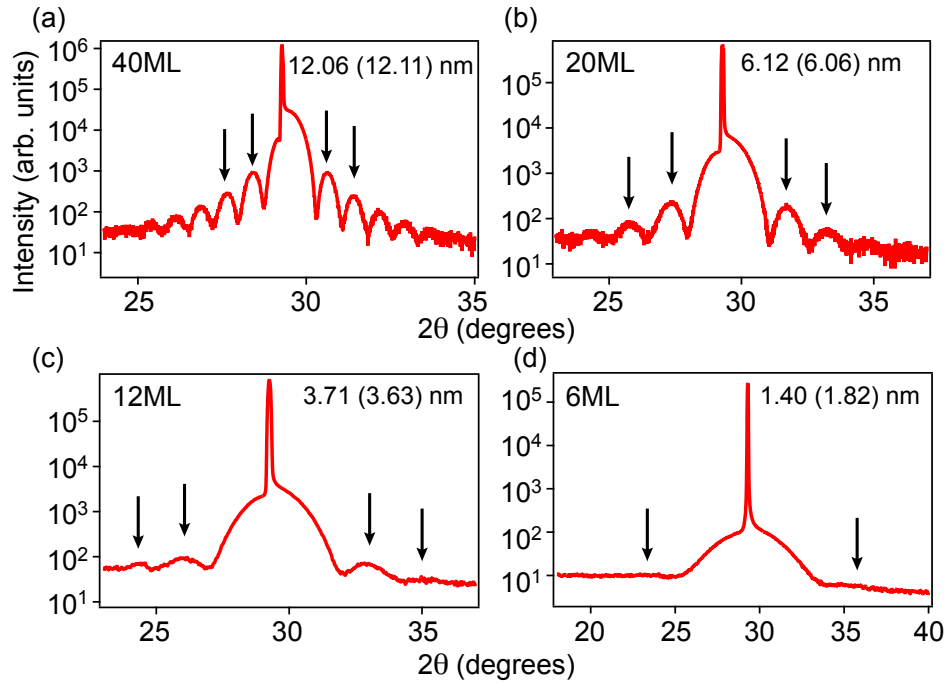


FIG. S1. **Estimation of film thickness from Keissig fringes** Out-of-plane  $\theta - 2\theta$  x-ray diffraction scans around LuSb (002) Bragg peak showing Keissig fringes for (a) 40ML (b) 20ML (c) 12ML (d) 6ML thick films. Black arrows indicate the Keissig fringes that were utilized for the estimation of film thickness. Estimated film thickness and corresponding nominal thickness (in brackets) are marked in each panel showing excellent correspondence between the two.

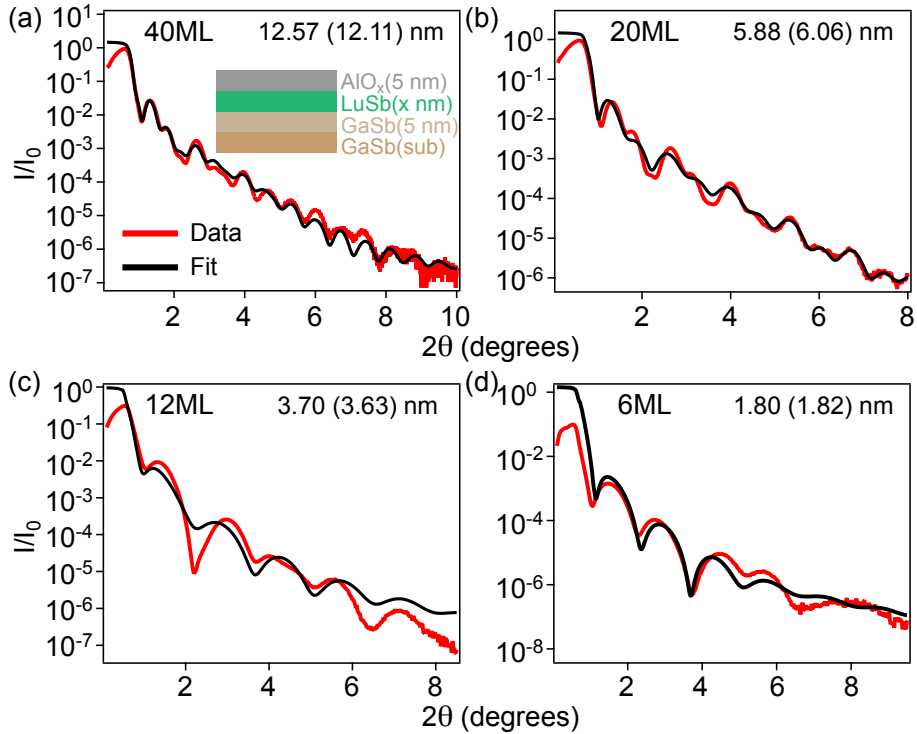


FIG. S2. **Estimation of film thickness from x-ray reflectivity** X-ray reflectivity data and corresponding fits for (a) 40ML (b) 20ML (c) 12ML (d) 6ML thick films. Sample structure along with nominal thicknesses of each layer is shown in the inset of panel (a). Estimated film thickness and corresponding nominal thickness (in brackets) are marked in each panel showing excellent correspondence between the two.

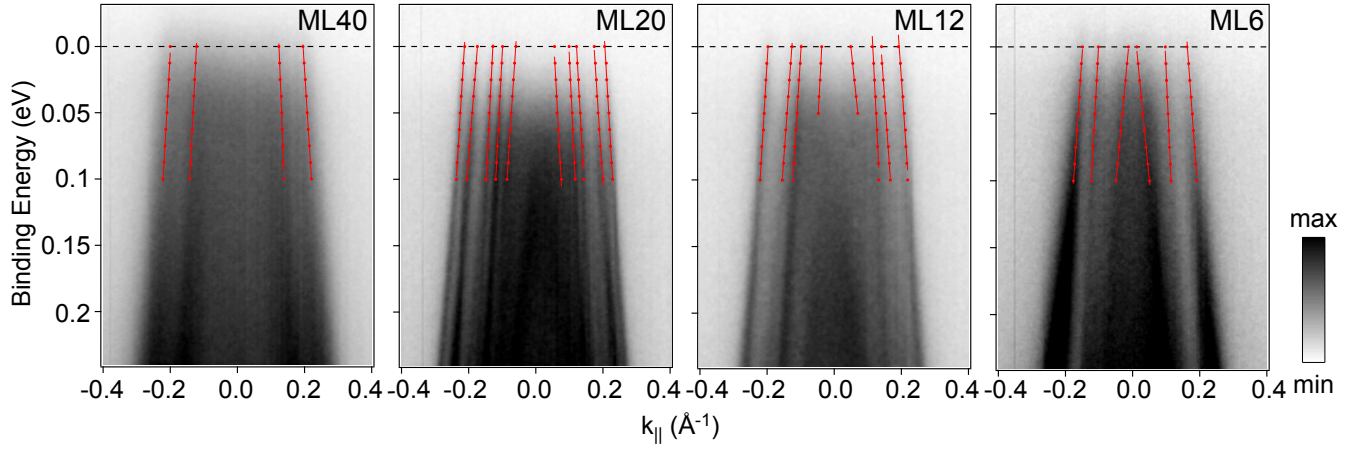


FIG. S3. **Extraction of Fermi wavevector ( $k_F$ ) and Fermi velocity ( $v_F$ ) from ARPES data** ARPES data along  $\bar{M} - \Gamma - \bar{M}$  at the bulk  $\Gamma$  point taken at 70K for (a) 40ML (b) 20ML (c) 12ML (d) 6ML thick films. Extracted dispersions and corresponding fits are shown in red.

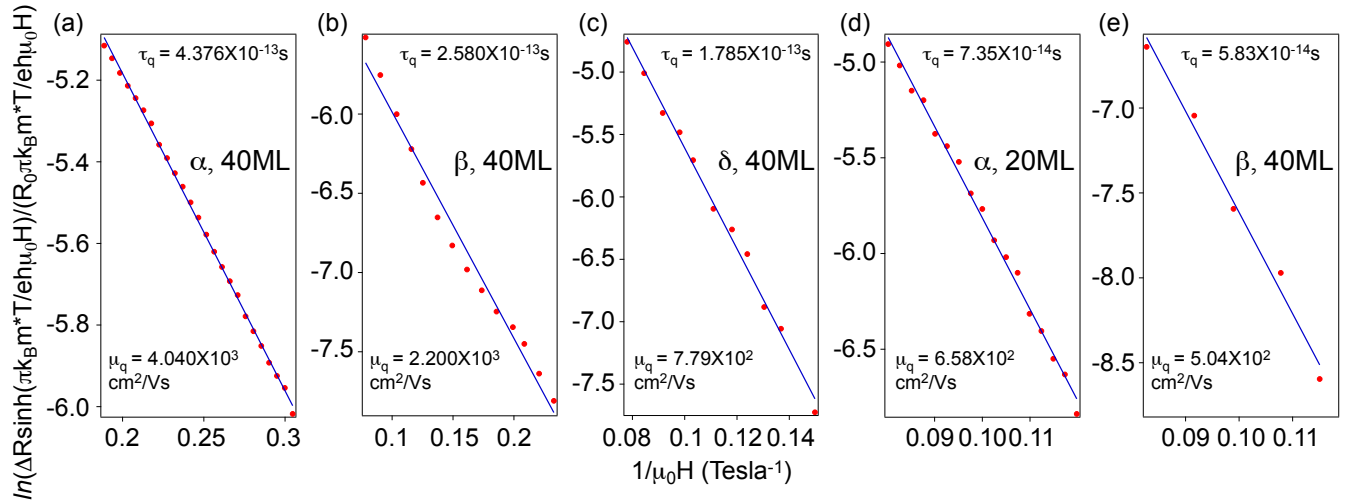


FIG. S4. **Quantum mobility of carriers in LuSb thin films** Quantum mobility is calculated from the linear slope of the fits for (a)  $\alpha$  (b)  $\beta$  (c)  $\delta$  Fermi pocket for 40ML thick film and (a)  $\alpha$  (b)  $\beta$  pocket for 20ML thick film. Quantum mobility ( $\mu_q$ ) and corresponding lifetime ( $\tau_q$ ) values are marked in the corresponding panels.

- [8] Chatterjee, S. *et al.* Weak antilocalization in quasi-two-dimensional electronic states of epitaxial LuSb thin films. *Physical Review B* **99**, 125134 (2019).
- [9] Nummy, T. J. *et al.* Measurement of the atomic orbital composition of the near-fermi-level electronic states in the lanthanum monopnictides labi, lasb, and laas. *NPJ Quantum Materials* **3**, 24 (2018).

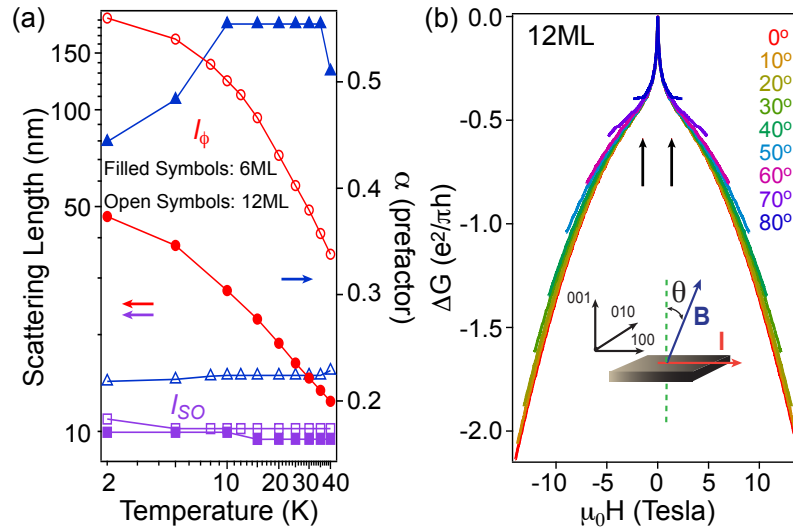


FIG. S5. **Quantum corrections to transport data in ultra-thin LuSb films** (a) Phase coherence and spin-orbit scattering lengths as a function of temperature for both 12 and 6ML thick films. While phase coherence length is reduced significantly at higher temperatures, spin-orbit scattering length roughly remains independent of temperature. The value of the pre-factor  $\alpha$  is  $\approx 0.5$  for 6ML thick film as expected for a strongly spin-orbit coupled single two-dimensional channel. (b) Angle dependent magnetoresistance data for 12ML thick film showing angular scaling behavior expected for a two-dimensional electronic system between magnetic field of  $\pm 1$  Tesla.

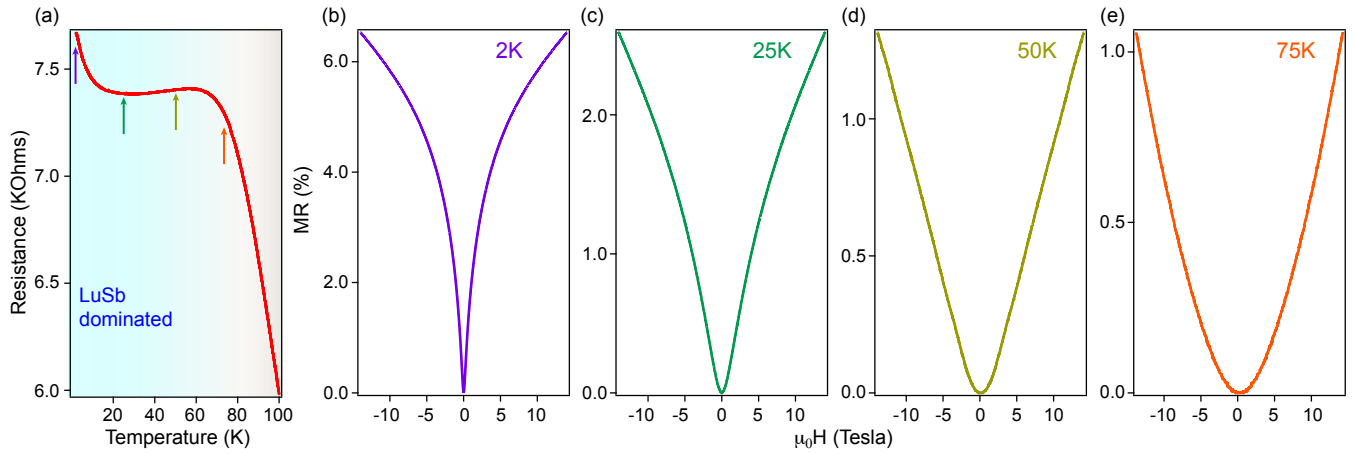


FIG. S6. **Evolution of magnetoresistance with temperature in the 6ML thick LuSb film.** (a) Temperature dependence of resistance of the 6ML thick film. Temperature region dominated by LuSb atomic layers when carriers from underlying GaSb layers freeze out is highlighted in blue. Magnetoresistance behavior at (b) 2K (c) 25K (d) 50K (e) 75K. Temperatures at which magnetoresistance data is obtained are highlighted in panel (a). At higher temperatures magnetoresistance evolves from saturating behavior to non-saturating behavior as seen in thicker films underscoring the importance of electron-electron interaction effects in modifying magnetoresistance behavior at low temperatures in few atomic layer geometries.

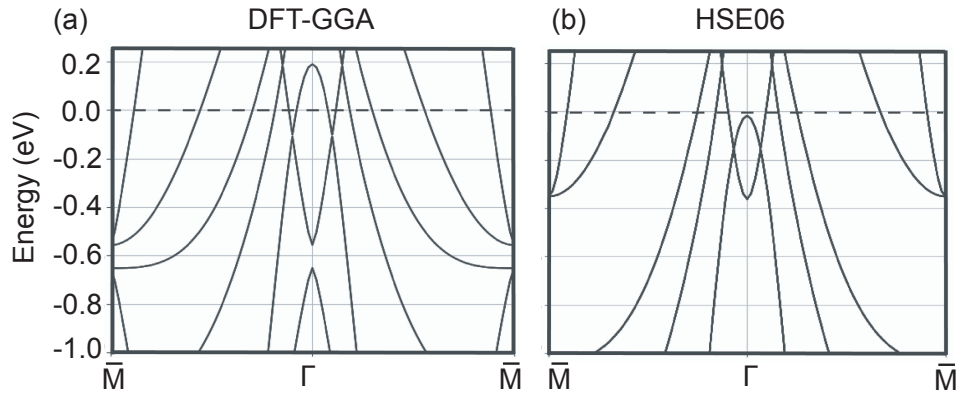


FIG. S7. **Electronic band structure of bulk LuSb for the 4 atom tetragonal cell.** Calculations made using (a) DFT-GGA and (b) HSE06 functional. In DFT-GGA the overlap between the electron and hole pockets are significantly overestimated, leading to an overestimation of the carrier density. The carrier density using the HSE06 functional is in good agreement with experimental data [8].

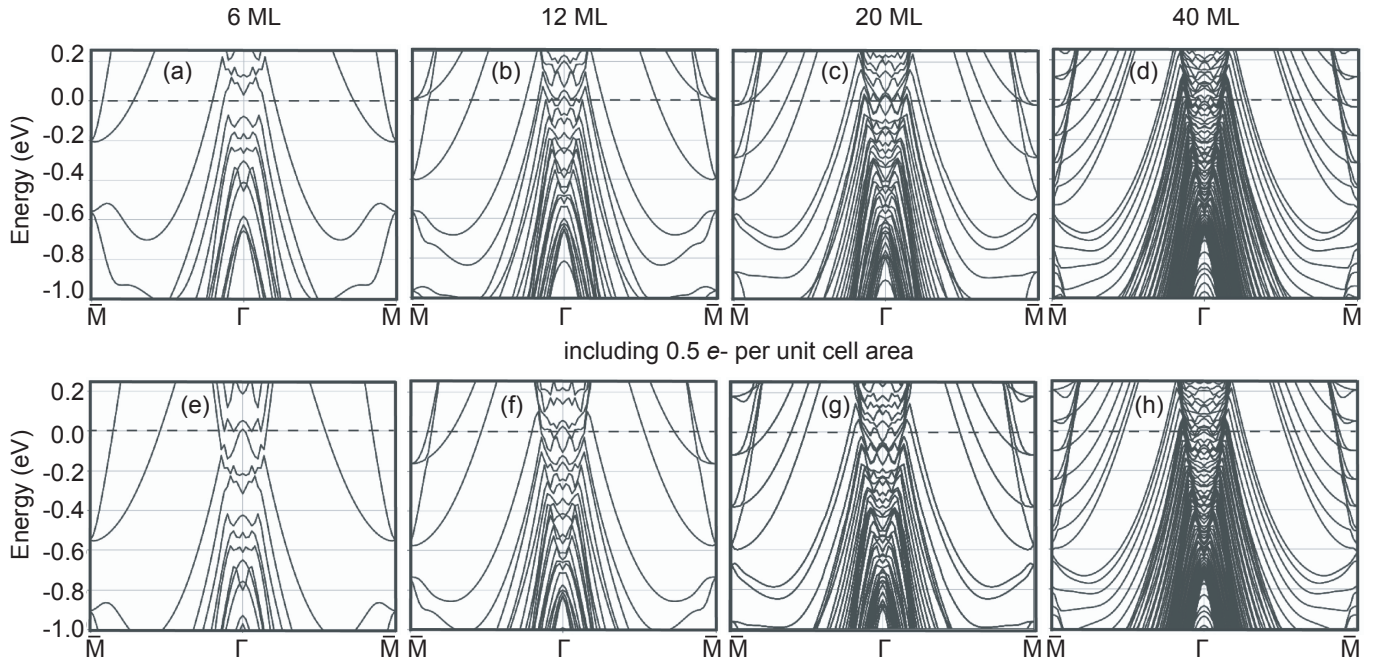


FIG. S8. **Calculated electronic structure of free-standing LuSb(001) films as a function of film thickness (number of monolayers or ML)** for (a) 6 ML, (b) 12 ML, (c) 20 ML, and (d) 40 ML. Corresponding electronic structure of LuSb(001) films in (e)-(f) after adding 0.5 electrons per unit cell area to account for excess charge at the interface between Ga terminated GaSb(001) and LuSb(001) atomic layers.

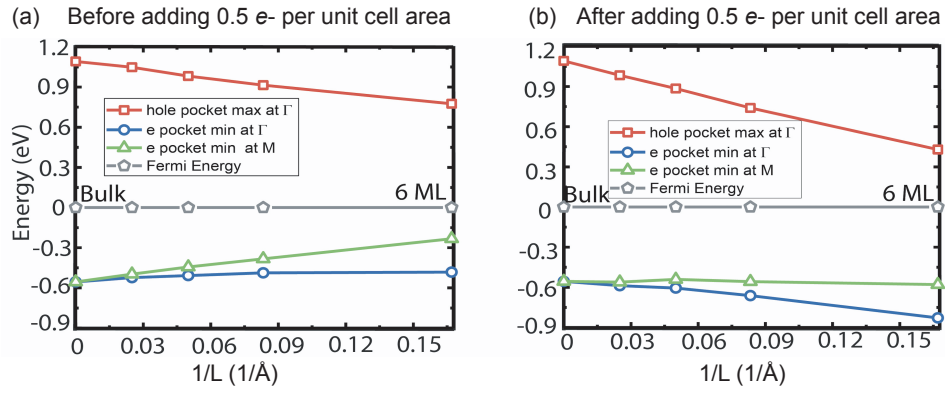


FIG. S9. **Position of the electron pocket minima and the hole pocket maxima with respect to the Fermi level as a function of the film thickness.** (a) Without any excess charge to the LuSb film, and (b) after adding 0.5 electron per unit cell area to the LuSb film to account for the excess charge at the interface between Ga terminated GaSb(001) and LuSb(001) atomic layers.

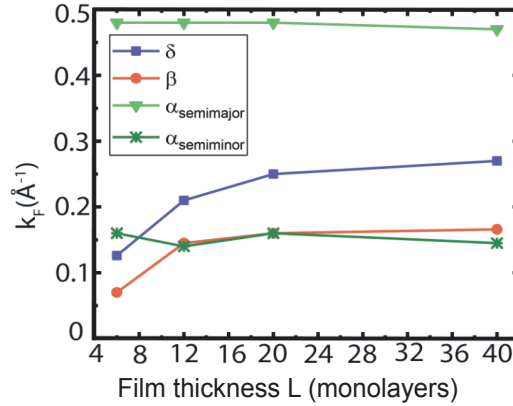


FIG. S10. **Calculated Fermi wavevectors after charge transfer.** Fermi wavevectors  $k_F$  associated with  $\alpha$ ,  $\beta$  and  $\delta$  pockets as a function of film thickness after adding 0.5 electron per unit cell area to the LuSb film to account for the excess charge at the interface between Ga terminated GaSb(001) and LuSb(001) atomic layers.